scientific reports

Check for updates

OPEN

Open complementary split-ring resonator-embedded tri-band rectangular monopole antenna with offset feed for next-gen wireless applications

S. Prasad Jones Christydass[1], Devakirubakaran Samithas[2]✉, Praveen Kumar Balachandran[3,5,6]✉ & Muhammad Ammirrul Atiqi Mohd Zainuri[4]

This paper presents the design and development of a compact tri-band rectangular monopole antenna tailored for Wireless Local Area Network (WLAN), Wireless Avionics Intra-Communications (WAIC), and Worldwide Interoperability for Microwave Access (WiMAX) applications. The antenna integrates an Open Complementary Split-Ring Resonator (OCSRR) etched onto the radiating patch and employs an offset microstrip feed to enhance impedance matching and multiband performance. Fabricated on an FR4 substrate (27.84 mm × 23.25 mm × 1.6 mm), the antenna achieves resonances at 3.16 GHz, 3.82 GHz, and 5.41 GHz. The OCSRR introduces a resonance at 3.16 GHz by exhibiting negative permittivity, verified through the Nicolson-Ross-Weir (NRW) method. Ground plane reduction and offset feeding contribute to additional resonances and bandwidth enhancement. The antenna demonstrates strong agreement between simulated and measured results, with reflection coefficient of − 19.83 dB, − 17.9 dB, and − 55.73 dB, and impedance bandwidths of 180 MHz, 190 MHz, and 2750 MHz, respectively. Radiation patterns remain stable across all bands, with peak gains of 2.19 dBi, 2.27 dBi, and 2.82 dBi. The proposed antenna offers a low-profile, high-performance solution for next-generation wireless systems requiring compact size, multiband operation, and reliable performance.

Keywords OCSRR, Metamaterial, Tri-band, Offset feed, WLAN, WAIC, WiMAX.

Modern wireless communication systems demand far more high data rates, small device size, and consistent multiband performance than they did years ago. As WLAN, WiMAX, WAIC, RADAR, and 5G/6G systems continue to expand rapidly, antennas able to support multiband and wideband operations have become absolutely essential for providing high-speed, effective communication[1,2]. Thus, a key field of research to fulfil the changing needs of modern wireless technologies is the construction of small, efficient, and reasonably priced multiband antennas[3–5]. Using slots[6], defected ground structures (DGS)[7], fractal geometries[8], and metamaterial-inspired designs such split ring resonators (SRR), complementary split ring resonators (CSRR), and electric-LC (ELC) resonators[9–12] various antenna structures have been investigated to achieve multiband performance. These techniques frequently suffer from complex geometry, higher fabrication difficulties, large physical dimensions, and lower gain even if they have been successful in some situations[13,14]. Particularly small resonator structures such as the open complementary split-ring resonator (OCSRR), metamaterials present a possible substitute by allowing multiband operation with reduced electrical size and improved control of electromagnetic properties[15–18]. Since Wi-Fi (IEEE 802.11a/n/ac/ax), wireless avionics intra-communications (WAIC), WLAN, and future 5G services[19–21] make extensive use of the 5 GHz frequency range, it was chosen as the design focus

[1]School of Electronics Engineering, Vellore Institute of Technology, Chennai, Tamilnadu 600127, India. [2]Department of Automobile Engineering, SRM Institute of Science and Technology, Kattankulathur, Chennai, Tamilnadu 603203, India. [3]Department of Electrical and Electronics Engineering, Vardhaman College of Engineering, Hyderabad, TG, India. [4]Department of Electrical, Electronic and Systems Engineering, Faculty Engineering and Built Environment, Universiti Kebangsaan Malaysia, 43600 Bangi, Selangor, Malaysia. [5]Department of Electrical and Electronics Engineering, Chennai Institute of Technology, Chennai, Tamilnadu, India. [6]Centre for Research Impact and Outcome, Chitkara University Institute of Engineering and Technology, Chitkara University, Rajpura, Punjab, India. ✉email: kirubathas@gmail.com; praveen@ukm.edu.my

for this work. To support the high throughput and dependability of these applications, antennas running in the 5 GHz range must be highly efficient, have wide bandwidth, and produce steady radiation patterns. Moreover, reaching multiband operating around the 5 GHz region improves spectrum use and device flexibility.

Metamaterials are structures with dimensions smaller than the wavelength of electromagnetic waves, and thus exhibit unconventional electromagnetic properties, such as negative values of parameters like ε (permittivity), μ (permeability), and η (impedance). Metamaterials have attracted significant attention from academics in recent decades due to their exceptional electromagnetic characteristics. These distinctive characteristics enable researchers to create innovative electromagnetic devices and components. The distinctive characteristics arise from its arrangement rather than its components. A key research gap still exists in obtaining compact, planar antennas that simultaneously offer multiband resonance, large impedance bandwidth, and simple fabrication without compromising gain or radiation properties[22,23], despite much study. These distinctive electromagnetic properties have a constructive effect on the propagation of electromagnetic waves[24–27]. The metamaterial must meet the requirement of having a unit cell size equal to P<ʎg/4. The many types of metamaterial structures commonly employed in antenna design for purposes such as impedance matching, size reduction, bandwidth enhancement, gain improvement, and directivity enhancement include SRR (Split Ring Resonator), S-shaped, CSRR (Complementary Split Ring Resonator) and ELC (Electric-LC)[28–32]. Conventions may fall short in combining minimal reflection coefficient in the 5 GHz range and down with compactness and multiband operation.

The major research challenges in this domain include:

- Achieving multiband resonance while maintaining compact antenna size,
- Ensuring efficient impedance matching across all operating bands,
- Maintaining high gain and stable omnidirectional radiation patterns,
- Simplifying the antenna structure to facilitate easy fabrication.

The Open Split Ring Resonator (OSRR) and its twin component are additional metamaterial structures that possess a compact electrical size. An Open Split Ring Resonator (OSRR) is the unenclosed variant of the Split Ring Resonator (SRR). Figure 1a and b illustrate the OSRR topology and its corresponding circuit diagram. Similarly, Fig. 1c and d illustrate the OCSRR architecture and its equivalent circuit. The series LC circuit is the equivalent circuit of OSRR. A split-ring resonator (SRR) is modified by opening it and then applying duality to create an open complementary split-ring resonator. The terminal refers to the metallic area that establishes an electrical connection between the slot rings and facilitates capacitive interaction within the slots. Hence the OCSRR is an open parallel resonant frequency as illustrated in Fig. 1d, and the resonant frequency of OCSRR equal to

$$f_0 = \frac{1}{2\,\Pi\,\sqrt{C_c\,L_0}} \tag{1}$$

The capacitance C_c is almost equivalent to the capacitance of the CSRR with the same dimension, whereas the inductance L_0 is larger than four times the inductance of the CSRR. Therefore, the electrical dimensions of the OCSRR will be halved in comparison to the CSRR. The resonant frequency is equivalent to half of the CSRR resonant frequency. Because of the tiny electrical dimension of OCSRR, it is possible to create a high-performance multiband antenna without increasing its size. However, the exploration of OSRR and OCSRR for achieving multiband functioning in antenna design is limited.

This article presents the design of a compact tri-band rectangular monopole antenna for multiband wireless applications. The OCSRR and decreased ground structure enable the proposed antenna to resonate at multiple frequencies. The OCSRR is responsible for generating the supplementary oscillation at a frequency of 3.16 GHz. The permittivity characteristic is obtained using the NRW approach and verified using the quasi-static analysis

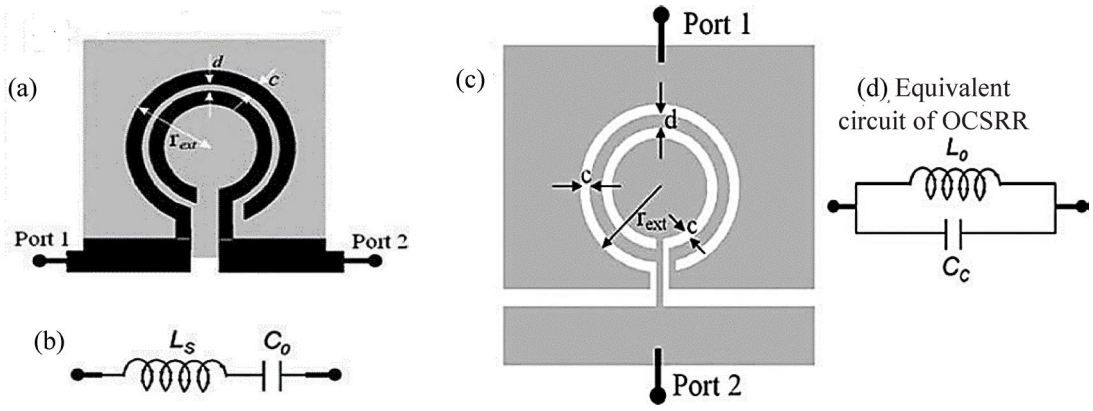

Fig. 1. Topologies and equivalent circuits of OSRR and OCSRR structures: (**a**) OSRR geometry, (**b**) equivalent circuit of OSRR, (**c**) OCSRR geometry, and (**d**) equivalent circuit of OCSRR.

of OCSRR. The report includes both data to confirm that the presence of OCSRR is responsible for the 3.16 GHz resonating bands. The antenna properties, including Gain, Current direction, E plane, and H plane, remain consistent with typical rectangular antennas due to the patch always being rectangular in shape. The suggested OCSRR inspired rectangular printed antenna is well-suited for multiband wireless applications due to its compact size, stable radiation properties, excellent gain, and easy fabrication.

The main contributions of this work are as follows:

- A novel compact tri-band antenna design utilizing an offset feed and OCSRR loading,
- Demonstration of negative permittivity behaviour in the OCSRR using waveguide S-parameter extraction,
- Systematic parametric study to optimize the critical dimensions affecting resonance,
- Validation of the proposed design through both simulation and experimental results,
- Comparison with state-of-the-art antennas to highlight the superior performance in terms of bandwidth, size, and multiband capability.

Furthermore, this text explores the development of the proposed rectangular antenna inspired by OCSRR. It includes an in-depth analysis of the process for extracting permittivity, conducting a parametric study, and establishing the equivalent circuit for the antenna. Section 3 presents a comprehensive review of the simulated and measured results to validate the proposed design, while Sect. 4 offers the concluding remarks of the article.

Materials and methods

Design of OCSRR inspired rectangular printed antenna

The rectangular printed antenna presented is fabricated on a substrate composed of FR4, a material with a dielectric constant of 4.4. Figure 2 illustrates the many stages of the antenna design process carried out using CST software. The antenna undergoes three stages of development. The geometric structure of the rectangular printed antenna, inspired by OCSRR, is illustrated in Fig. 3. The corresponding parameter values may be found in Table 1.

The Ant A, which is a rectangular monopole, is powered by a 50 Ω microstrip feed and functions at a frequency of 5 GHz. Next, the concept of offset feed is introduced during the second stage of evolution in order to obtain optimal impedance matching. Ant B is designed with a shortened ground length of 3 mm. The Ant B is utilized to produce dual-band resonance at frequencies of 5.5 and 3.82 GHz. Next, the suggested framework is created by incorporating the OCSRR developed at a frequency of 3.12 GHz in the area with the highest surface current. The dimensions of the antenna are 27.84 mm x 23.25 mm x 1.6 mm, where each size is a fraction of the free space wavelength (λ_0) at a frequency of 5 GHz (f_0). Specifically, the dimensions are $0.464\,\lambda_0 \times 0.3875\,\lambda_0 \times 0.0267\,\lambda_0$. This rectangular printed antenna, based on the OCSRR design, operates at three specific frequency bands: 3.16 GHz, 3.82 GHz, and 5.41 GHz.

Ant A is a printed seed antenna on a FR4 substrate. It consists of a rectangular patch with a width of wp and a length of lp. The other side of the substrate has a full ground with a width of ws and a length of ls. Ant A is constructed via Eqs. 2–5. The antenna design exhibits resonance at a frequency of 5 GHz, and its operational bandwidth spans from 4.87 GHz to 5.08 GHz.

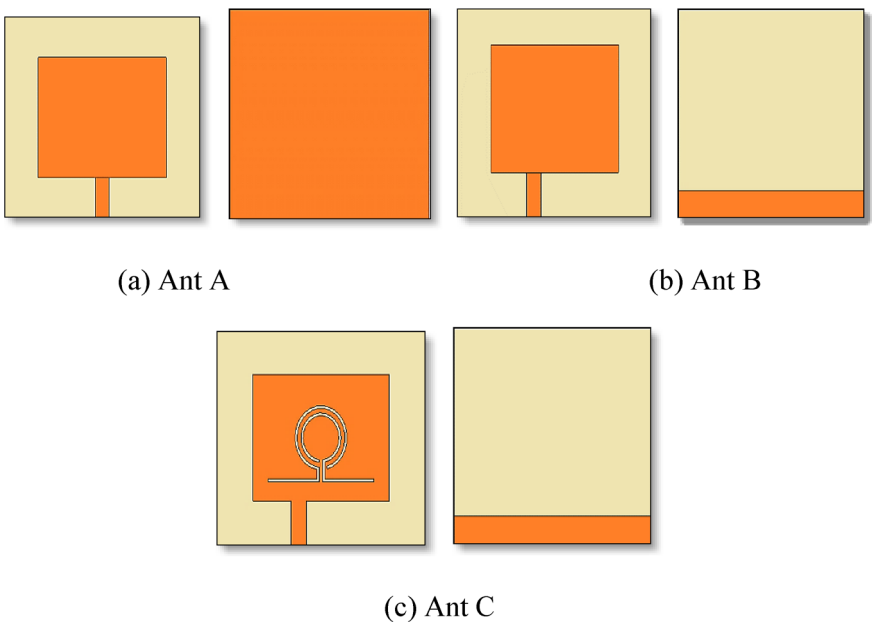

Fig. 2. Design evolution stages of the proposed tri-band antenna: (**a**) Ant A—basic rectangular monopole, (**b**) Ant B—offset-fed monopole with reduced ground, and (**c**) Ant C—final design with OCSRR integration.

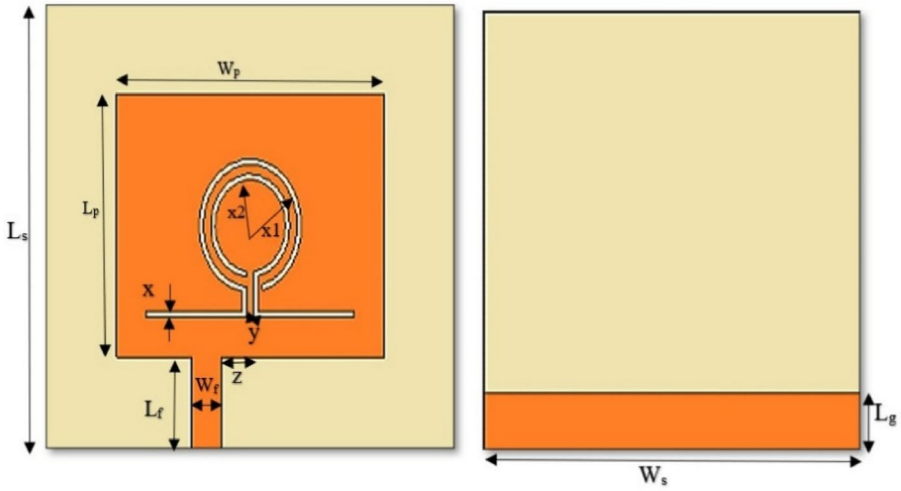

Fig. 3. Front and back views of the proposed tri-band offset-fed rectangular monopole antenna with OCSRR and its parameters.

Parameter	W_s	L_s	W_p	L_p	x	L_g
Dimension (mm)	27.84	23.25	18.24	13.75	0.3	3
Parameter	y	x1	x2	W_f	L_f	z
Dimension (mm)	1	3.5	2.7	2	4.75	3.5

Table 1. Tri-band offset feed OCSRR resonator etched rectangular monopole parameters. All dimensions are in millimeters.

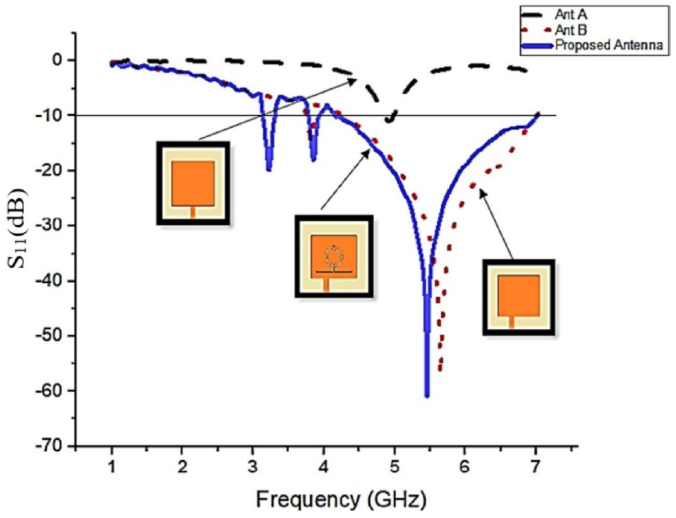

Fig. 4. Comparison of simulated return loss ($|S_{11}|$ in dB) for Ant A, Ant B, and the proposed tri-band antenna, showing the impact of offset feeding and OCSRR loading.

$$W = \frac{c}{2f_r}\sqrt{\frac{2}{\epsilon_r + 1}} \tag{2}$$

$$L = \frac{c}{2f_r\sqrt{\epsilon_{eff}}} - 2\Delta L \tag{3}$$

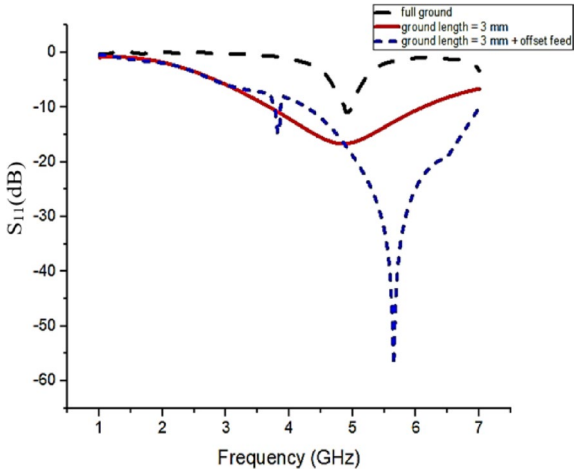

Fig. 5. Parametric analysis of ground plane length on return loss performance, highlighting the optimal ground length for multiband operation.

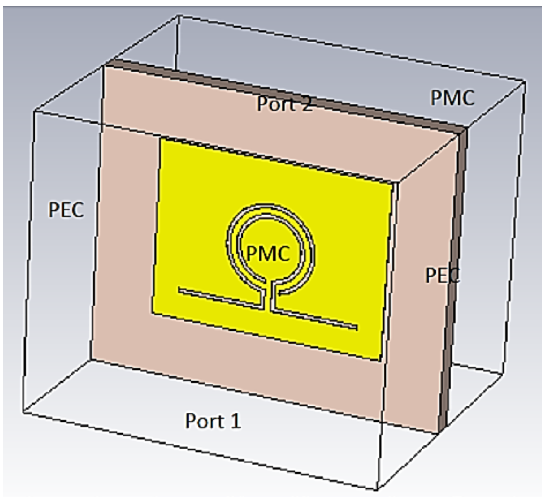

Fig. 6. Waveguide simulation setup in CST for extracting S-parameters of the OCSRR using PEC and PMC boundary conditions.

$$\epsilon_{eff} = \frac{\epsilon_r + 1}{2} + \frac{\epsilon_r - 1}{2}\left[1 + \frac{12h}{W}\right]^{\frac{-1}{2}} \tag{4}$$

$$\Delta L = 0.412h \frac{(\epsilon_{eff} + 0.3)}{(\epsilon_{eff} - 0.258)} \frac{\left(\frac{W}{h} + 0.264\right)}{\left(\frac{W}{h} + 0.8\right)} \tag{5}$$

The variables in the equation are defined as follows: ccc represents the speed of light, fr denotes the resonance frequency, h is the height of the dielectric substrate used in the design, and ϵ_{eff} is the effective dielectric constant of the substrate. Shifting the feed to the left enhances impedance matching, which is crucial for the antenna's performance. Reducing the size of the ground plane improves the impedance bandwidth at 5 GHz and introduces an additional resonance at 3.8 GHz. This careful adjustment significantly impacts the antenna's functionality, making it more versatile.

Ant B exhibits dual-band resonance at frequencies of 3.8 GHz and 5.7 GHz, demonstrating its capability to operate effectively in multiple bands. The OCSRR (Open Complementary Split Ring Resonator) is specifically designed to function at 3.14 GHz and is strategically placed in the area with the highest surface current. This optimal positioning generates an additional resonance at 3.16 GHz, enhancing the antenna's overall performance. The final design of the OCSRR-based rectangular printed antenna is engineered to operate in three distinct frequency bands: 3.16 GHz, 3.82 GHz, and 5.41 GHz. The antenna covers frequency ranges of 3.14 to 3.30 GHz, 3.79 to 3.93 GHz, and 4.15 to 7.01 GHz, with reflection coefficient values of -19.17 dB, -17.18 dB, and −55.8 dB, respectively. These low reflection coefficient values indicate excellent impedance matching and minimal reflection, crucial for efficient antenna operation.

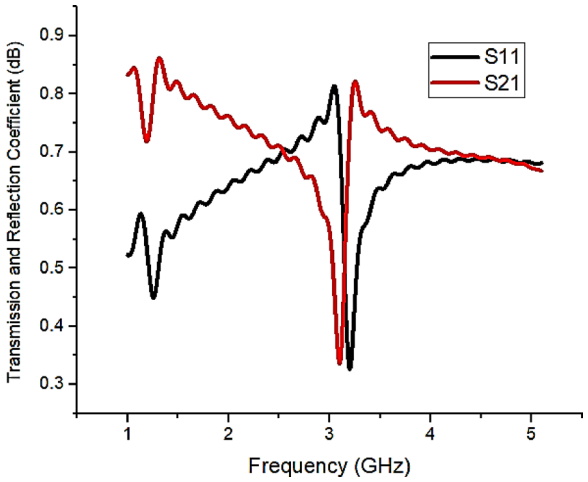

Fig. 7. Simulated reflection (S11) and transmission (S21) coefficients of the OCSRR, showing resonance at 3.16 GHz.

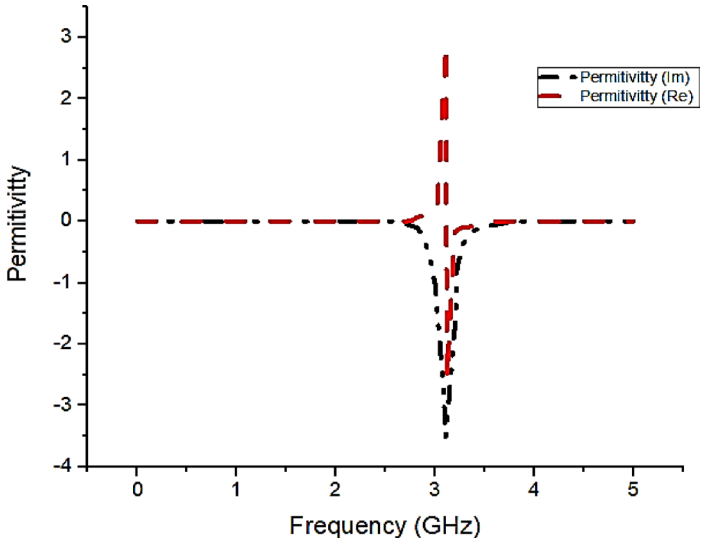

Fig. 8. Extracted permittivity characteristics of the OCSRR using the NRW method, confirming negative permittivity near 3.16 GHz.

Figure 4 illustrates the reflection coefficient values for different design stages of the OCSRR-based rectangular printed antenna. The inclusion of OCSRR resulted in the clear observation of a new resonance at 3.16 GHz, significantly improving the antenna's performance. Additionally, the impedance in all other resonating bands was reasonably matched, confirming the effectiveness of the design adjustments. Shifting the feed to the left greatly improves impedance matching in the proposed antenna design because of the improved ground structure and asymmetric surface current distribution resulting from the OCSRR etching. The OCSRR's insertion and the ground size decrease produce a distorted current distribution throughout the patch, therefore concentrating the strongest surface currents away from the geometric centre. The feed point lines more closely to the area of optimal surface current by shifting the feed towards the left, therefore ensuring that the local input impedance naturally fits the 50 feed line. Without extra matching networks, this change reduces reflection losses and improves power transfer efficiency. Furthermore, by essentially stimulating several resonant modes, the leftward offset not only enhances impedance matching at the principal resonant frequency (around 5 GHz) but also generates an extra resonance at 3.82 GHz. As so, the antenna achieves effective multiband operation covering 3.16 GHz, 3.82 GHz, and 5.41 GHz bands with enhanced impedance bandwidth. The comprehensive analysis and iterative design process ensure that the proposed antenna meets the desired specifications and performs reliably across the specified frequency bands.

Figure 5 presents a comparison of the simulated reflection coefficientfor various ground lengths. It is evident that a ground length of 3 mm, along with an offset feed, achieves excellent impedance bandwidth matching and introduces a new frequency band. The parametric analysis of the antenna, with a diminished ground length of

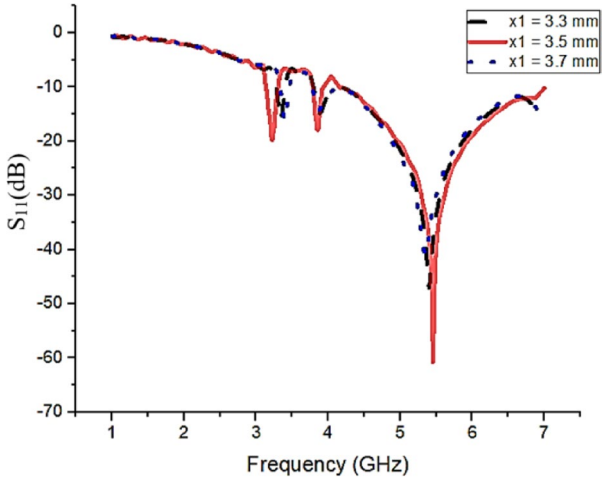

Fig. 9. Parametric analysis of outer ring radius (x1) on return loss.

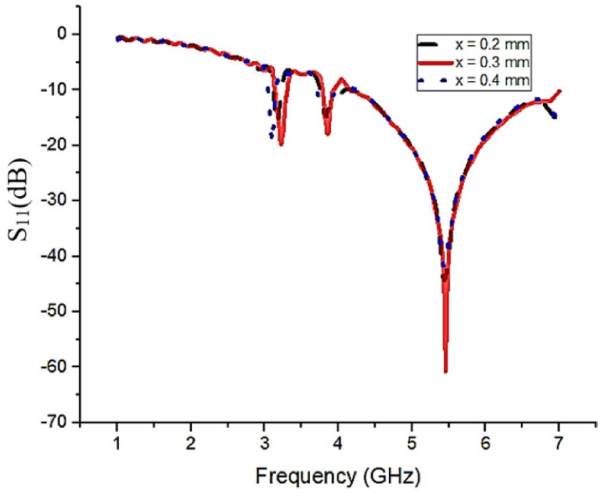

Fig. 10. Parametric analysis of ring width (x) on return loss, showing its influence on impedance matching.

3 mm, demonstrates a substantial effect on its electromagnetic performance. The complete ground structure demonstrates inadequate impedance matching, with S11 remaining over − 10 dB throughout the operational band. When the ground is diminished to 3 mm, a significant enhancement in the reflection coefficient is observed, attaining values below − 20 dB around 5 GHz, signifying improved resonance and energy coupling. The introduction of offset feed, combined with the 3 mm reduced ground, significantly improves performance, attaining a deep resonance below − 50 dB around 5.5 GHz and augmenting the operational fractional bandwidth. This arrangement enhances gain performance by reducing ground plane length, which improves radiation efficiency and decreases surface wave losses. The integration of diminished ground and offset feed results in a modest elevation of the resonant frequency due to modified current pathways, while simultaneously broadening the bandwidth by decreasing the Q-factor.

Analysis of the OCSRR and its permittivity extraction

The OCSRR is etched onto a rectangular radiating element in the suggested final arrangement, resulting in an additional resonance at 3.16 GHz. The SRR resonant frequency can be determined using Eq.

$$f_{csrr} = \frac{c}{2\Pi}\sqrt{\frac{3(x_2 - x_1 - w)}{Re\,(\epsilon_r)\,x_1^3}} \tag{6}$$

The resonant frequency of the Open Complementary Split Ring Resonator (OCSRR) is exactly half of the resonant frequency of the Conventional Split Ring Resonator (CSRR). This relationship arises from the unique structure and properties of the OCSRR, which is designed to exhibit resonances that are harmonically related to those of the CSRR.

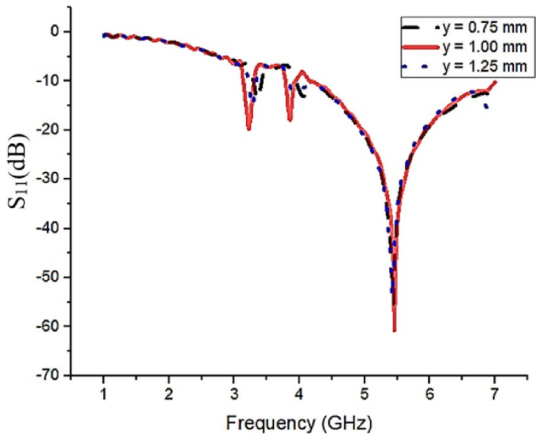

Fig. 11. Parametric analysis of slot spacing (y) on return loss.

Parameter	Values simulated	Optimal value	Observation
x1	3.3 mm, 3.5 mm, 3.7 mm	3.5 mm	Improved S_{11} matching at 3.16 GHz
x	0.2 mm, 0.3 mm, 0.4 mm	0.3 mm	Stable S_{11} across bands
y	0.75 mm, 1.00 mm, 1.25 mm	1.0 mm	Improved S_{11} matching at 3.16 GHz

Table 2. Optimum values of OCSRR and its observations.

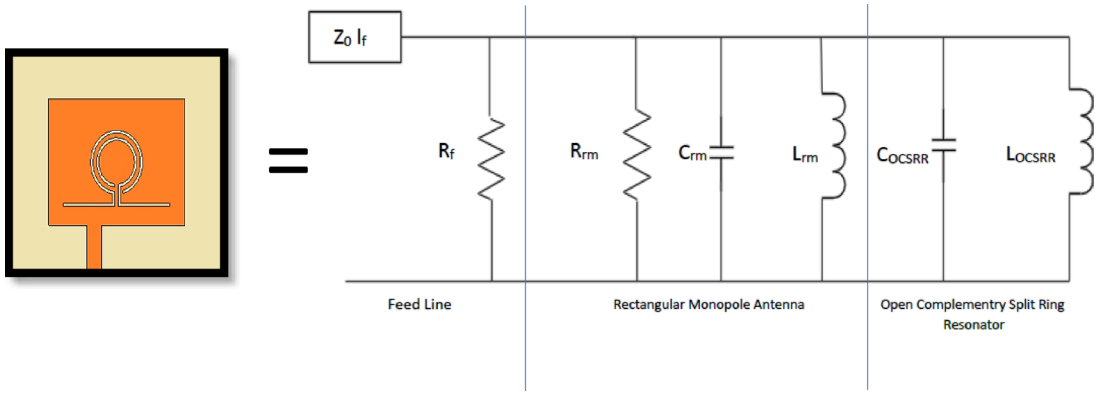

Fig. 12. Equivalent circuit model of the proposed tri-band antenna including OCSRR elements, modelled using parallel RLC branches.

Mathematically, the resonant frequency f_{OCSRR} of the OCSRR can be determined using the formula: $f_{OCSRR} = 0.5 \times f_{CSRR}$.

Here, f_{CSRR} represents the resonant frequency of the CSRR. By halving this value, we obtain the resonant frequency of the OCSRR. This relationship is fundamental in the design and analysis of metamaterial structures and allows for precise tuning of the resonant frequencies to achieve desired electromagnetic properties.

$$f_{ocsrr} = \frac{c}{4\Pi}\sqrt{\frac{3(x_2 - x_1 - w)}{Re\,(\epsilon_r)\,x_1^3}} \tag{7}$$

In the context of the electromagnetic structure being discussed, the variables are defined as follows: x2 represents the radius of the outer ring slot, x1 represents the radius of the inner ring slot, and w represents the width of the ring. These variables play a crucial role in determining the resonant frequencies of the Split Ring Resonator (SRR) and the Open Complementary Split Ring Resonator (OCSRR).When specific values are assigned to these variables, such as x1(inner slot radius) as 2.7 mm and x2 (outer slot radius) as 3.5 mm, we can apply Eqs. 6 and 7 to calculate the resonant frequencies of the SRR and OCSRR. Substituting these values into the equations yields a resonant frequency of 6.28 GHz for the SRR and a resonant frequency of 3.14 GHz for the OCSRR.

Freq (GHz)	Zr (real) (Ω)	Zim (Imag) (Ω)
3.22	33.78	1.67
3.85	41.56	1.43
5.45	57.1	2.56

Table 3. Real and imaginary impedances.

Freq (GHz)	*R* (ohm)	L (pH)	C (pF)
3.22	33.78	82.54	29.6
3.85	41.56	59.11	28.9
5.45	57.1	74.75	11.4

Table 4. Resistor (R), inductor (L), and capacitor (C) values for each resonating frequency.

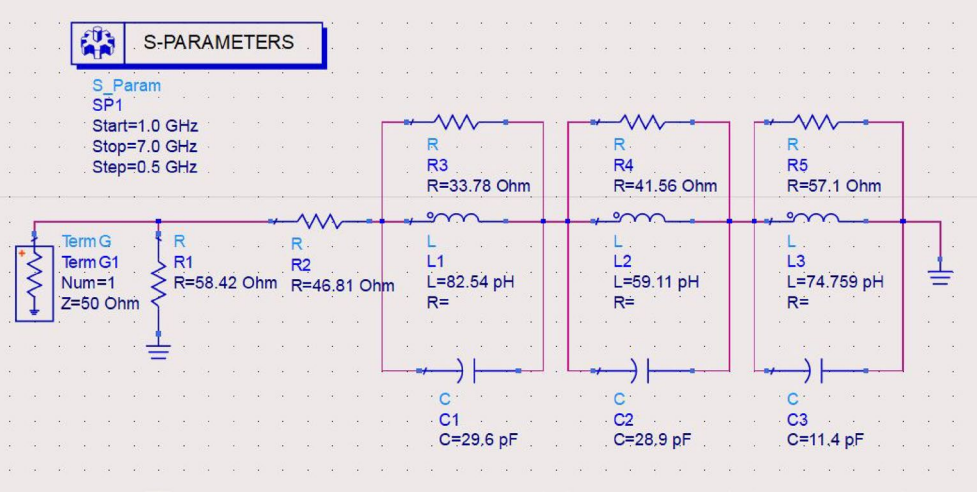

Fig. 13. Simulated equivalent circuit of the proposed antenna in ADS, representing tri-band behavior.

$$f_{\mathrm{OCSRR}} = \frac{1}{2\pi\sqrt{L_{\mathrm{OCSRR}} C_{\mathrm{OCSRR}}}}$$

$$f_{\mathrm{OCSRR}} = \frac{1}{4\pi\sqrt{L_{\mathrm{CSRR}} \cdot C_{\mathrm{CSRR}}}} = \frac{1}{2} f_{\mathrm{CSRR}}$$

$$\Rightarrow f_{\mathrm{OCSRR}} = \frac{1}{2} \cdot 6.28\,\mathrm{GHz} = 3.14\,\mathrm{GHz}$$

Figure 6 illustrates the waveguide configuration used to obtain the S parameters of the Open Complementary Split Ring Resonator (OCSRR) within the CST simulation environment. The waveguide setup includes Perfect Electric Conductor (PEC) and Perfect Magnetic Conductor (PMC) boundary conditions, ensuring accurate simulation results. Upon stimulation by an electromagnetic wave entering through the input port, the OCSRR's reflection and transmission coefficients are determined, as presented in Fig. 7. The passband characteristic of the OCSRR is identified at a frequency of 3.16 GHz, corroborated by calculating the resonant frequency using Eq. 6. These characteristics define the operational frequency range of the OCSRR, spanning from 3.14 GHz to 3.30 GHz. This analysis provides valuable insights into the OCSRR's performance and behaviour, crucial for designing and optimizing the proposed antenna.

Figure 8 shows the negative permittivity of OCSRR, which was determined using the NRW method as described in reference[27].

$$\mathrm{V}_1 = \mathrm{S}_{21} + \mathrm{S}_{11} \tag{8}$$

$$\mathrm{V}_2 = \mathrm{S}_{21} - \mathrm{S}_{11} \tag{9}$$

$$\mathrm{S}_{11} = \mathrm{re}\,(\mathrm{S}_{11}) + \mathrm{j}\,(\mathrm{im}\,(\mathrm{S}_{11})) \tag{10}$$

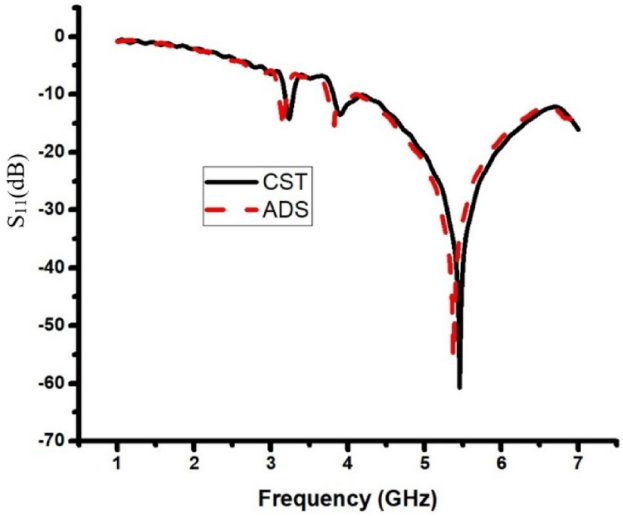

Fig. 14. Comparison of reflection coefficient between CST full-wave simulation and ADS circuit model, validating the equivalent circuit.

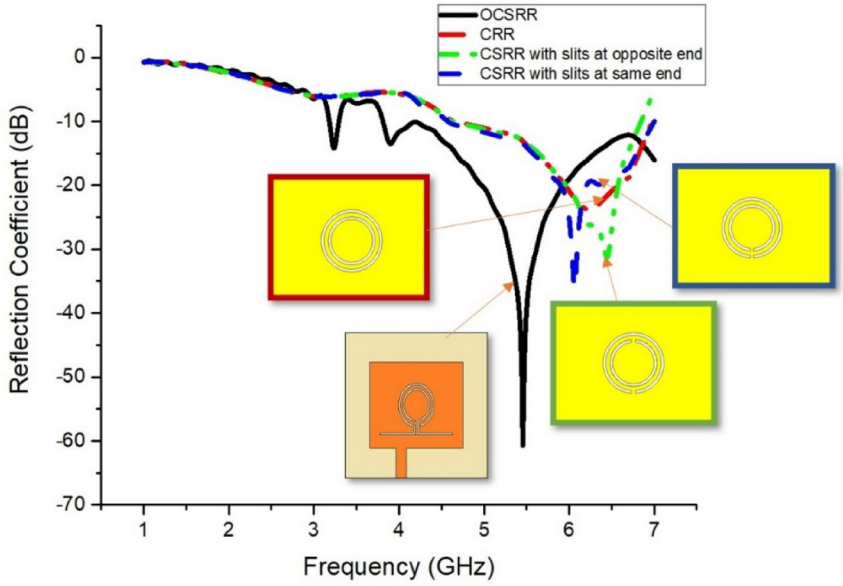

Fig. 15. Comparison of reflection coefficient between OCSRR and various CSRR configurations.

$$S_{21} = \mathrm{re}\,(S_{21}) + \mathrm{j}\,(\mathrm{im}\,(S_{21})) \tag{11}$$

$$\mu = \frac{2}{jK_O d} * \frac{1 - V_2}{1 + V_2} \tag{12}$$

$$\epsilon = \frac{2}{jK_O d} * \frac{1 - V_1}{1 + V_1} \tag{13}$$

The code is executed using MATLAB. The negative permittivity is determined by analyzing the S_{11} reflection characteristics and S_{21} transmission characteristics of the specified OCSRR, which are obtained by simulation and extracted from the CST software. The OCSRR being considered has a negative permittivity at a frequency of 3.16 GHz.

Parametric analysis of OCSRR

The optimal values of the critical parameters of the OCSRR are determined by parametric analysis in CST software. The final proposed structure undergoes parametric analysis. The radius of the outer ring (x1) is

changed incrementally from 3.3 to 3.7 mm, with a step size of 0.2 mm. Figure 9 displays the simulated reflection coefficientplot for several values of x1. Upon examination of the figure, it is evident that x1 = 3.5 mm exhibits favourable impedance matching throughout all resonant bands, with a noticeable frequency shift occurring in the 3.16 GHz region. Therefore, it may be inferred that the OCSRR is accountable for the frequency of 3.16 GHz.

Subsequently, the diameter of the ring, denoted as x, is augmented from 0.2 to 0.4 mm. The resulting simulated reflection coefficient values are then compared in Fig. 10. The increment is performed in increments of 0.1 mm, and it is noteworthy that at x = 0.3 mm, there is optimal impedance matching across all resonant bands. The OCSRR causes a change in frequency. Figure 11 illustrates the comparison of reflection characteristics for various values of y. The value of y has been incremented from 0.75 to 1.25 mm in increments of 0.25 mm. This change has also impacted the 3.16 GHz band, indicating that the presence of OCSRR is responsible for this frequency band. The value y = 1 mm exhibits excellent impedance matching across all resonant bands without compromising bandwidth. As a result, it is selected for the final production. Tabl2 2 preents the optimum values of the OCSRR and it observations (Table 2).

Equivalent circuit of OCSRR inspired rectangular monopole

Figure 12 displays the analogous circuit of the rectangular printed antenna, which is inspired by the OCSRR. Z_0 and lf represent the characteristic impedance (50 Ω) and electrical length of the transmission line, respectively. R_f denotes the resistance that is associated with losses. The R_{rm}, C_{rm}, and L_{rm} elements are utilized to depict the rectangular monopole antenna. The elements C_{OCSRR} and L_{OCSRR} are utilized to symbolize the OCSRR that is etched in the rectangular monopole. The inductance, L_{OCSRR}, is caused by the conductive metal region located between the slots. The capacitance, C_{OCSRR}, arises from the capacitance across the slots. The resonant frequency of an OCSRR is equivalent to

$$f_0 = \frac{1}{2\,\Pi\,\sqrt{C_{OCSRR}\,L_{OCSRR}}} \tag{14}$$

Representing the suggested microstrip patch antenna as a parallel combination of a resistor (R), an inductor (L), and a capacitor (C), one can obtain the resonant behaviour of the antenna. The equivalent circuit model of the antenna is made of three separate parallel RLC branches, each matching to one of the resonances since the antenna is made to run at three different resonant frequencies. These RLC circuits emulating the multi-resonant character of the antenna are linked in parallel.The circuit-level representation was developed using Advanced Design System (ADS) software to precisely depict this behaviour. Full-wave simulations carried out with CST Microwave Studio allowed one to recover both real and imaginary components of the input impedance at each resonance. These impedance values are given in Table 3 and form the basis for lumped circuit parameter computation.

Using the conventional resonance relationships, the lumped component values—resistance (R), inductance (L), and capacitance (C)—for each resonant branch were calculated: $Q = 2\pi f_r CR$ and $f_r = (1/2\pi(LC)\text{^}(1/2))$, The resonance frequency is f_r; the quality factor is Q. The component values were computed methodically using these formulas and the CST-derived impedance values; they are compiled in Table 4.

From your Table 3, for the 3.22 GHz band (close to 3.16 GHz), the extracted values are:L = 82.54 pH.

- L = 82.54 pH.
- C = 29.6 pF.

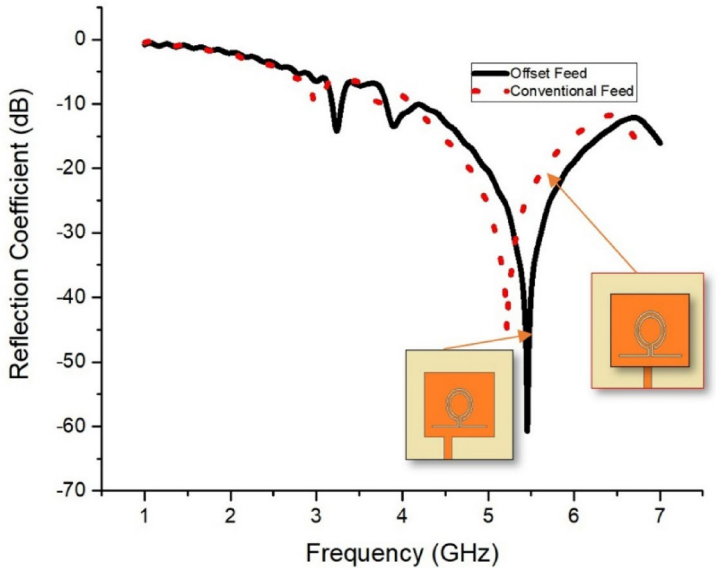

Fig. 16. Comparison of reflection coefficient between conventional centre feed and offset feed.

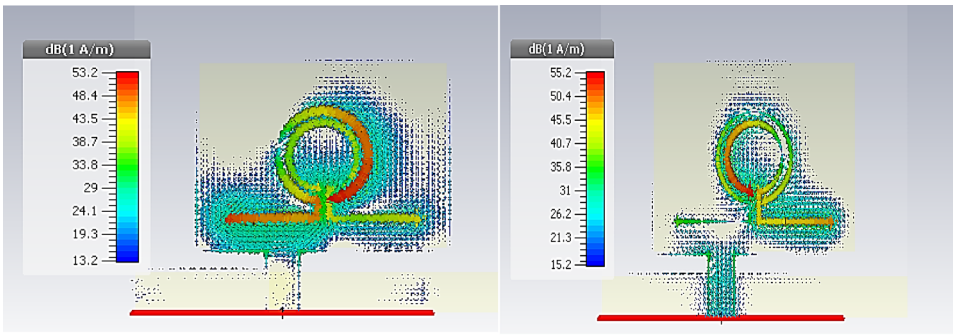

a) 3.16 GHzb)3.82 GHz

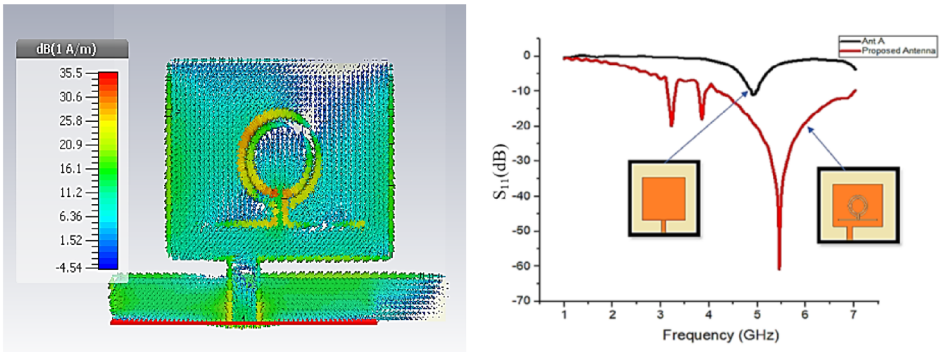

c) 5.41 GHz d) Ant A Vs Tri-Band Offset

Fig. 17. Surface current distribution at resonant frequencies: (**a**) 3.16 GHz, (**b**) 3.82 GHz, (**c**) 5.41 GHz, and (**d**) return loss comparison between Ant A and the proposed antenna.

$$f = \frac{1}{2\pi\sqrt{LC}} = \frac{1}{2\pi\sqrt{(82.54 \times 10^{-12})(29.6 \times 10^{-12})}} = 3.24\,\text{GHz}$$

This also agrees closely with the measured value of 3.16 GHz, verifying the actual physical resonance based on your extracted lumped parameters.The whole equivalent circuit was built and simulated within ADS using these computed R, L, and C values (Fig. 13). The simulated S-parameters derived from this circuit model were then matched with those from the CST full-wave simulations and the recorded experimental data. Figure 14 shows a clear link between the CST Model and the circuit model. Moreover, the resistance values were precisely changed to get ideal impedance matching at every resonant frequency, therefore guaranteeing correct emulation of the performance of the antenna over the designated ranges.

The Open Complementary Split Ring Resonator (OCSRR) surpasses the Conventional CSRR in both theoretical and simulation contexts. The OCSRR oscillates at half the frequency of the CSRR due to its open configuration. The equation fOCSRR = 0.5 × fCSRR demonstrates this. When x_1 = 2.7 mm and x_2 = 3.5, the CSRR operates at a frequency of 6.28 GHz, whereas the OCSRR functions at 3.14 GHz. Th use of OCSRR introduces a resonance at 3.16 GHz. This indicates that OCSRR is superior for contemporary antenna applications due to its small design, enhanced impedance matching, and multi-band functionality. The simulation of CSRR various configuration presented in Fig. 15 also indicates the OCSRR will have lower resonant frequency due to increase in the effective capacitance, which is the result of split.

The Open Complementary Split Ring Resonator (OCSRR) surpasses the Conventional CSRR in both theoretical and simulation contexts. The OCSRR oscillates at half the frequency of the CSRR due to its open configuration. The equation fOCSRR = 0.5 × fCSRR demonstrates this. When $x1$ = 2.7 mm and $x2$ = 3.5, the CSRR operates at a frequency of 6.28 GHz, whereas the OCSRR functions at 3.14 GHz. Th use of OCSRR introduces a resonance at 3.16 GHz. This indicates that OCSRR is superior for contemporary antenna applications due to its small design, enhanced impedance matching, and multi-band functionality. The simulation of CSRR various configuration presented in Fig. 15 also indicates the OCSRR will have lower resonant frequency due to increase in the effective capacitance, which is the result of split.

The Fig. 16 demonstrate that the offset feed creates excitation asymmetry, facilitating enhanced coupling between the feed and the resonant structure. This design stimulates supplementary modes, optimises surface current distribution, and reduces the Q-factor, consequently augmenting bandwidth. In contrast to traditional feeding methods, the offset feed markedly enhances impedance matching, attaining deeper resonance and a

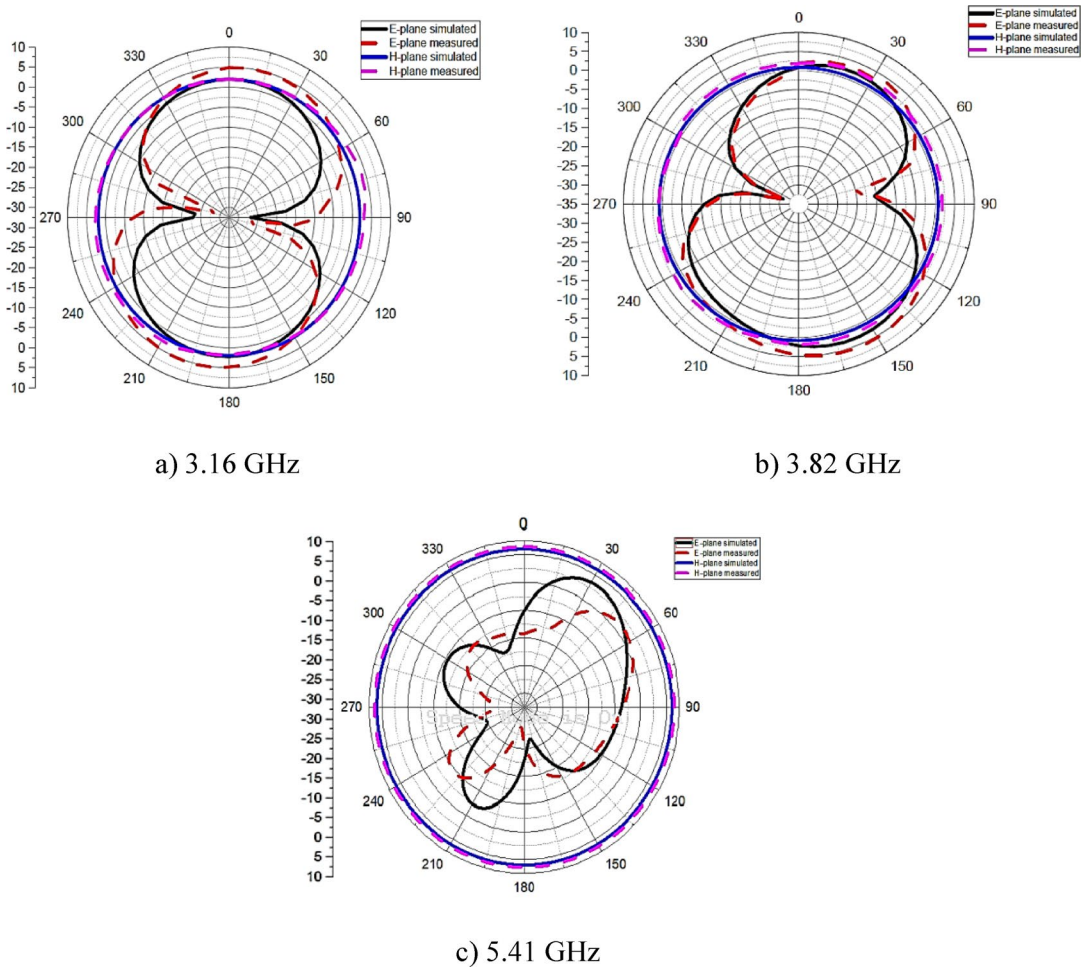

Fig. 18. Measured and simulated radiation patterns in E-plane and H-plane at (**a**) 3.16 GHz, (**b**) 3.82 GHz, and (**c**) 5.41 GHz.

broader bandwidth around 5 GHz. This enhancement is essential for contemporary multiband and wideband antenna applications, providing superior performance without modifying the antenna's physical dimensions.

Result and discussion

The figure labelled as Fig. 17 displays the current distribution at the resonating band. It is evident from the figure that the surface current reaches its highest value when centred at the OCSRR at a frequency of 3.16 GHz. The distribution of surface current clearly indicates that the OCSRR is accountable for the 3.16 GHz frequency, whereas its impact on the 3.82 GHz frequency is insignificant. The surface current is uniformly distributed across the entire antenna at a frequency of 5.41 GHz. Figure 8 shows that the OCSRR exhibits a negative permittivity at a frequency of 3.14 GHz, indicating that it possesses the characteristics of an ENG metamaterial. Therefore, we can infer that the engraved OCSSR is responsible for the frequency of 3.16 GHz. Furthermore, the validation is conducted by analysing the OCSRR, as outlined in Sect. 2.2.

Figure 17ddisplays the simulation return loss plot of Ant A and the planned OCSRR inspired rectangular Antenna. The graphic shows that a single band Ant A has been improved to function at three different frequency bands, with a wide range of impedance and good matching in all of these bands. The achievement is made possible with the use of a smaller ground, feeding the element at a different position, and incorporating an OCSRR at the radiating element. Figure 18 presents a comparison between the measured E-plane and H-plane with their corresponding simulated values. A consistent radiation pattern is achieved throughout all resonant bands. The E plane exhibits a dipole pattern in the shape of an eighth, while the H plane displays a radiation pattern that is omnidirectional. Figure 19 displays the image of the created antenna. The antenna that was created is evaluated using the VNA Anritsu S820E. The antenna under test (AUT) was set on a precision-controlled rotating positioner for radiation pattern and gain measurements; a standard calibrated horn antenna was the transmitting antenna. Maintaining a 1.5-meter distance between the AUT and the transmitting antenna, the far-field condition matching the highest working frequency of the antenna was satisfied. High-performance radio-frequency absorption materials lined the chamber walls so precisely as to simulate free-space circumstances. To enable exact angle scans in both the E-plane and the H-plane, all measurements were automated and timed with the positioner and the VNA.The obtained measurements are then compared to the simulated results, which are

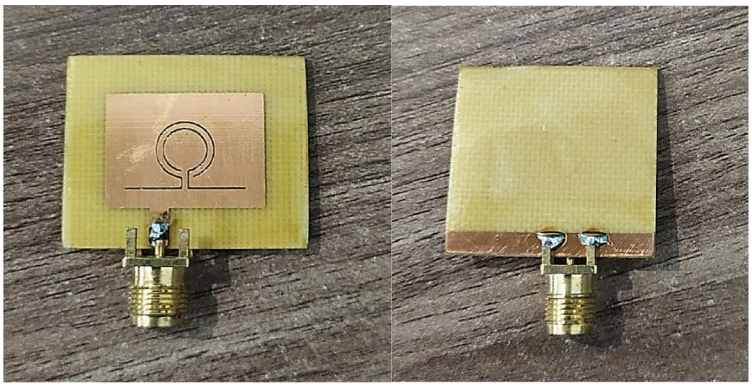

a) Front and Back View of the proposed antenna

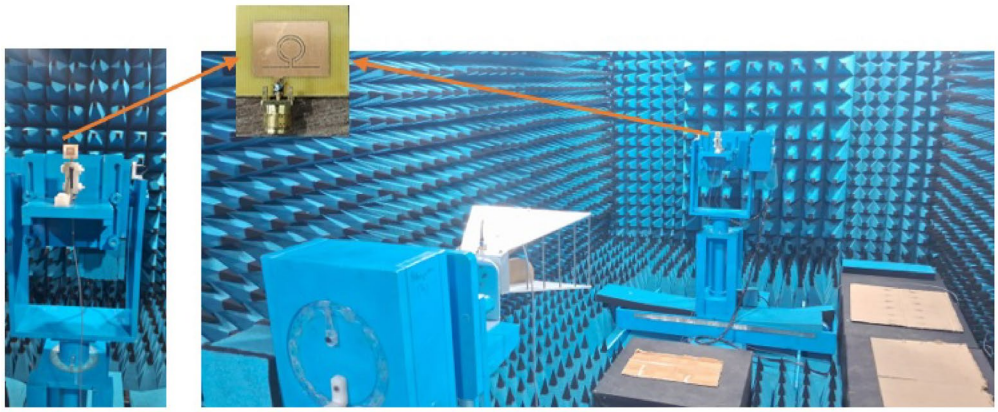

b) Anechoic Camber Measurement Environment

Fig. 19. Photographs of the fabricated antenna prototype and the anechoic chamber measurement setup.

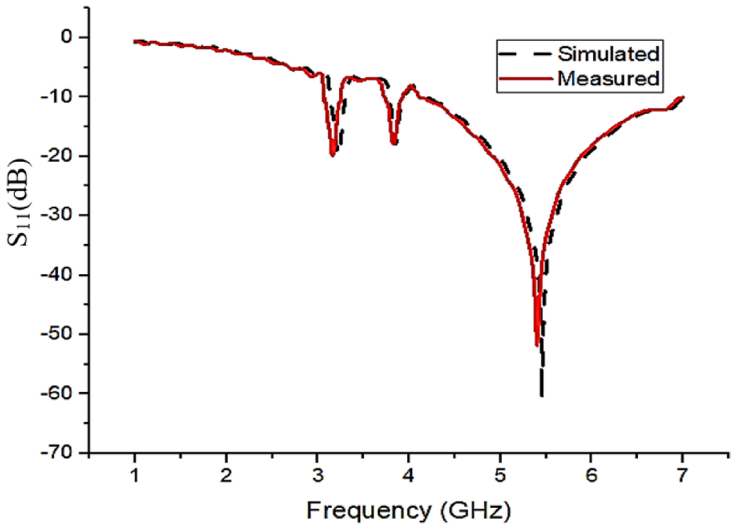

Fig. 20. Comparison of simulated and measured return loss (|S11| in dB) for the proposed antenna.

Simulated				Measured			
Centre frequency (GHz)	Operating band (GHz)	Reflection coefficient (dB)	Impedance bandwidth (MHz)	Centre frequency (GHz)	Operating band (GHz)	Reflection coefficient (dB)	Impedance bandwidth (MHz)
3.22	3.14 to 3.30	− 19.71	160	3.16	3.07 to 3.25	− 19.83	180
3.85	3.79 to 3.89	− 17.67	100	3.82	3.73 to 3.92	− 17.9	190
5.45	4.15 to 7.00	− 60.725	2850	5.41	4.10 to 6.85	− 55.73	2750

Table 5. Measured vs. simulated results.

Ref. no.	Procedure used	L * W (mm^2)	Centre frequency (GHz)	Analysis of equivalent circuit	Verification of metamaterial property
[2]	Hexagonal patch, fractal	75 × 75	1.575, 5.9,7.2	Not presented	NA
[8]	Triangular patch, slot	30 × 28	1.6, 2.8, 5.7,9.6	Not presented	NA
[9]	Cresent shape patch	31 × 35	11.30, 18.07, 20.72	Not presented	NA
[11]	Fractal, L shape slot and SRR	30 × 24.8	3.3, 5.5, 7.3,9.9	Not presented	Not Presented
[12]	U slot	30 × 40	1.8, 2.4,3.5	Not presented	NA
[13]	SRR	22 × 24	2.48, 3.49	Not presented	Not presented
[24]	QWSIW, fractal, CSRR	23 × 20.5	Between 4.96 to 5.88 (tunable by rotating the CSRR)	Not presented	Not presented
[25]	CSRR and reduced ground	20 × 25	4.5, 8	Not presented	Not presented
[27]	Slot, ELC, Koch Fractal	40 × 40	1.5, 3.5, 5.4	Not presented	Not presented
[26]	ELC	35 × 35	3.77, 5.4	Not presented	Not presented
[33]	Slot	18.65 × 14	10	Not presented	Presented
[34]	DRA	50.01 × 50.01	5.8	Presented	Not presented
[35]	Fractal, CSRR	35.94 × 38.97	3.62, 7.82 and 10.58	Not presented	Not presented
[36]	Double-layered FSS-backed miniaturized microstrip antenna with dipole strip array reflector	12.7 × 12.7	3.5 and 5.7	Presented	Presented
[37]	TFSA + FSS + reflector	30 × 30	3.15–4.20 and 4.38–7.03	Presented	Presented
OCSRR inspired rectangular antenna (proposed)	Offset feed, OCSRR	27.84 × 23.25	3.16, 3.82, 5.41	Presented	Presented

Table 6. Comparison between various antenna in the literature and tri-band offset feed OCSRR resonator etched rectangular monopole.

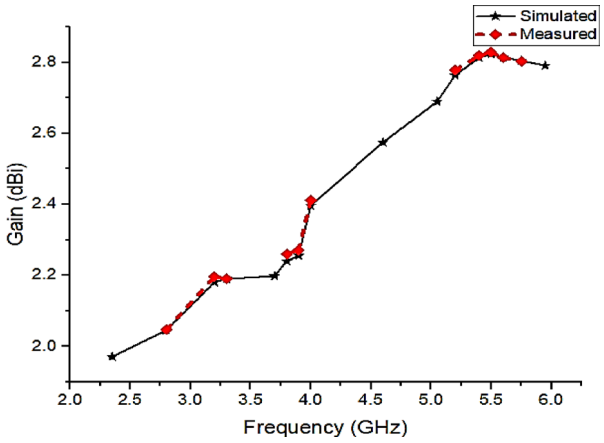

Fig. 21. Measured and simulated gain of the proposed antenna at 3.16 GHz, 3.82 GHz, and 5.41 GHz.

displayed in Fig. 20. The results exhibit a little discrepancy caused by fabrication fault and the soldering of the SMA connector.

In Table 5, measured values are compared with the simulated results, and in Table 6, the OCSRR inspired rectangular printed antenna is compared with the antenna which ispreviously available in the literature.

Figure 21 displays the measured and computed gain of the rectangular printed antenna inspired by OCSRR. At frequencies of 3.16, 3.82, and 5.41 GHz, the maximum peak gains are observed to be 2.19, 2.27, and 2.82 dBi, respectively.

The obtained three bands of the proposed antenna offer significant advantages across various RF applications. The 3.07 –3.25 GHz band (180 MHz) covers parts of the 3.1–3.3 GHz range, which is utilized in WiMAX, early 5G trials, and defense communication systems. This band provides excellent propagation characteristics, making it ideal for urban and indoor wireless networks. The 3.73 –3.92 GHz band (190 MHz) falls within the 3.5–3.8 GHz C-band, a globally important frequency range for 5G mid-band deployments. It offers a strong balance between coverage and capacity, and is widely used for 5G New Radio (NR) across various regions. Finally, the 4.10 –6.85 GHz band (2750 MHz) encompasses several crucial frequencies, including the unlicensed 5 GHz Wi-Fi bands (e.g., 5.15–5.85 GHz), sub-6 GHz 5G bands, and the ISM band (Industrial, Scientific, and Medical), along with supporting fixed satellite services, radar systems, and some military applications. The wide bandwidth of this band supports high data rate transmission, making it ideal for high-throughput applications such as video streaming, industrial automation, and advanced sensing systems.

Conclusion

A rectangular monopole with an open complementary split resonator is proposed. The tiny structure resonates at three frequencies. Resonating frequencies are 3.16, 3.82, and 5.41 GHz. It is found that measured reflection coefficient, gain, E-plane, and H-plane radiation pattern findings match simulated results. Parametric analysis identifies essential OCSRR dimensions and presents results. The OCSRR's negative permittivity is extracted using waveguide extraction. The negative permittivity at 3.14 GHz is verified by OCSRR resonant frequency calculation in Sect. 2.2. The proposed OCSSR-inspired rectangular printed antenna has an impedance bandwidth of 180 MHz (3.07 –3.25 GHz), 190 MHz (3.73 –3.92 GHz), and 2750 MHz (4.10 –6.85 GHz). The consistent radiation pattern, reasonable gain, simple construction, compactness, and tri-band properties make the suggested structure appropriate for wireless applications such RADAR, long-distance radio communication, WLAN, WAIC, and WiMAX.

Data availability

The datasets generated during and/or analysed during the current study are presented in the article.

Received: 15 January 2025; Accepted: 9 September 2025
Published online: 13 October 2025

References

1. Balanis, C. A. Antenna Theory. Antenna Theory Analysisi and Design. https://doi.org/10.1002/9780470661369.ch4 (2010).
2. Tripathi, D., Srivastava, D. K. & Verma, R. K. Bandwidth enhancement of slotted rectangular wideband microstrip antenna for the application of WLAN/WiMAX. *Wireless Pers. Commun.* 0123456789 https://doi.org/10.1007/s11277-021-08257-x (2021).
3. Ab Rashid, A. H., Ahmad, B. H. & Abd Aziz, M. Z. A. CPW fractal antenna with third iteration of pentagonal Sierpinski gasket Island for 3.5 ghz wimax and 5.2 ghz WLAN applications. *Int. J. Electr. Comput. Eng. Syst.* **14**(2), 129–134 (2023).
4. Khaleel, A. D., Rahem, A. A., razak, T., Mansor, B., Chakrabarty, C. K. & M. F., & Design tri-band rectangular patch antenna for Wi-Fi, Wi-Max and WLAN in military band applications with radiation pattern suppression. *Res. J. Appl. Sci. Eng. Technol.* **10**(12), 1445–1448. https://doi.org/10.19026/rjaset.10.1847 (2015).
5. Naqvi, A. H. & Lim, S. Low-profile electronic beam-scanning metasurface antenna for Ka-band applications. *Waves Random Complex. Media*, 1–16. (2023).
6. Rhazi, Y. et al. Novel design of multiband microstrip patch antenna for wireless communication. *Adv. Sci. Technol. Eng. Syst.* **4**(3), 63–68. https://doi.org/10.25046/aj040310 (2019).
7. Ali, T. & Biradar, R. C. A triple-band highly miniaturized antenna for WiMAX/WLAN applications. *Microw. Opt. Technol. Lett.* **60**(2), 466–471. https://doi.org/10.1002/mop.30993 (2018).
8. Praveen Chaurasia, B. K., Kanaujia, S., Dwari, M. K. & Khandelwal. Design and analysis of seven-bands-slot-antenna with small frequency ratio for different wireless applications. *Int. J. Electron. Commun.* (2018).
9. Ali, T., Muzammil Khaleeq, M. & Biradar, R. C. A multiband reconfigurable slot antenna for wireless applications. *AEU - Int. J. Electron. Commun.* **84**, 273–280. https://doi.org/10.1016/j.aeue.2017.11.033 (2018).
10. Raja, D. S. S. et al. A compact dual-feed wide-band slotted antenna for future wireless applications. *Analog Integr. Circuits Signal Process.* **118**(2), 291–305 (2024).
11. Tanweer Ali and Rajashekhar. C. Biradar.2017. A Compact multiband antenna using lamda/4 rectangular stub loaded with metamaterial for IEEE 802.11 N and IEEE 802.16E. *Microw. Opt. Technol. Lett.*, **59**(5).
12. Tanweer Ali, M. S. A. & R. C. B A fractal quad-band antenna loaded with L-shaped slot and metamaterial for wireless applications. *Int. J. Microw. Wirel. Technol.* **10**(7), 826–834 (2018).
13. Osama, W., Ata, M. & Salamin, K. A. Double U-slot rectangular patch antenna for multiband applications. *Comput. Electr. Eng.* **84**(1), 106–08. (2020).
14. Kumar Naik, K. Asymmetric CPW-fed SRR patch antenna for WLAN/WiMAX applications. *AEU - Int. J. Electron. Commun.* **93**(1), 103–108 (2018).
15. Pandeeswari, R. SRR and NBCSRR inspired CPW fed triple band antenna with modified ground plane. *Prog. Electromagnet. Res. C.* **80**, 111–118. https://doi.org/10.2528/pierc17101501 (2018).
16. Veselago, V. G. The electrodynamics of substances with simultaneously negative values of ε and μ. *Soviet Phys. Usphekhi.* **10**(4), 509–514 (1968).
17. Kong, J. A. Electromagnetic wave interaction with stratified negative isotropic media. *Progress Electromagnet. Res.* **35**, 1–52. https://doi.org/10.2528/PIER01082101 (2002).
18. Smith, D. R., Padilla, W. J., Vier, D. C., Nemat-Nasser, S. C. & S. S Composite medium with simultaneously negative permeability and permittivity. *Phys. Rev. Lett.* **84**, 4184–4187 (2000).

19. Chen, H., Wu, B. I. & Kong, J. A. Review of electromagnetic theory in left-handed materials. *J. Electromagn. Waves Appl.* **20**(15), 2137–2151. https://doi.org/10.1163/156939306779322585 (2006).
20. Pendry, J. B. Negative refraction makes a perfect lens. *Phys. Rev. Lett.* **85**(18), 3966–3969. https://doi.org/10.1103/PhysRevLett.85.3966 (2000).
21. Kumar, A. & Agrawal, T. High performance circularly polarized MIMO antenna with polarization independent metamaterial. *Wireless Pers. Commun.* **116**(4), 3205–3216. https://doi.org/10.1007/s11277-020-07843-9 (2021).
22. Singh, R. K. & Gupta, A. An asymmetric meandered line based dual-band ENG-TL antenna loaded with complementary closed ring resonators for gain enhancement. *IETE J. Res.* **69**(6), 3529–3539 (2023).
23. Wang, H., Qu, S., Yan, M., Zheng, L. & Wang, J. Design and analysis of dual-band polarization-selective metasurface. *Appl. Phys. A: Mater. Sci. Process.* **125**(11), 1–12. https://doi.org/10.1007/s00339-019-3013-y (2019).
24. Murugeshwari, B., Daniel, R. S. & Raghavan, S. A compact dual band antenna based on metamaterial-inspired split ring structure and hexagonal complementary split-ring resonator for ISM/WiMAX/WLAN applications. *Appl. Phys. A: Mater. Sci. Process.* **125**(9), 1–8. https://doi.org/10.1007/s00339-019-2925-x (2019).
25. Geetharamani, G. & Aathmanesan, T. Design of metamaterial antenna for 2.4 GHz WiFi applications. *Wireless Pers. Commun.* **113**(4), 2289–2300. https://doi.org/10.1007/s11277-020-07324-z (2020).
26. Elavarasi, C. & Shanmuganantham, T. SRR loaded CPW-fed multiple band rose flower-shaped fractal antenna. *Microw. Opt. Technol. Lett.* **59**(7), 1720–1724. https://doi.org/10.1002/mop.30609 (2017).
27. Herraiz-Martínez, F. J., Zamora, G., Paredes, F., Martín, F. & Bonache, J. Multiband printed monopole antennas loaded with OCSRRs for pans and WLANs. *IEEE Antennas. Wirel. Propag. Lett.* **10**, 1528–1531. https://doi.org/10.1109/LAWP.2011.2181309 (2011).
28. Hakim, M. L. et al. Triple-band square split-ring resonator metamaterial absorber design with high effective medium ratio for 5G sub-6 GHz applications. *Nanomaterials* **13**(2), 222. https://doi.org/10.3390/nano13020222 (2023).
29. Chowdhury, I. H. et al. Ultrawideband nanostructured metamaterial absorber with an Octagon-Packed Star-Shaped resonator for UV to NIR spectrum wavelength application. *Ain Shams Eng. J.* **15**(4), 102653 (2024).
30. Hasan, M. S. et al. Tunable asymmetric square split ring resonator based triple band metamaterial absorber for wireless communication system. *Opt. Mater.* **147**, 114746 (2024).
31. Jahan, M. I., Faruque, M. R. I. & Hossain, M. B. Flower-shape resonator-based triple-band metamaterial wave absorbers to find the dispersion relation utilizing one dimensional (1-D) periodic waveguide. *J. Magn. Magn. Mater.* **586**, 171202. (2023).
32. Ramachandran, T., Faruque, M. R. I. & Al-Mugren, K. S. Symmetric left-handed split ring resonator metamaterial design for terahertz frequency applications. *Sci Rep.* **13**(1), 21828. (2023).
33. Varshney, A. & Gençoğlan, D. N. Offset-fed slotted antenna practically loaded with split ring as water quality sensor for X-band industrial applications. *Adv. Electromagnet.* **13**(2), 39–52 (2024).
34. Mekki, S. et al. Design and investigation of orthogonal hybrid dual-mode single-CDR-based MIMO antenna with high self-isolation at 5.8 GHz. *IEEE Access* (2024).
35. Varshney, A. & Gençoğlan, D. N. High-gain multi-band koch fractal FSS antenna for Sub-6 ghz applications. *Appl. Sci.* **14**(19), 9022 (2024).
36. Ara, S., Kumari, N. P. & Varshney, A. Antenna miniaturization and application in-band interference reduction using dipole array mirror reflector FSS for sub 6 GHz applications. *Phys. Scr.* **100**(3), 035517 (2025).
37. Varshney, A. et al. Compact metasurface antenna for Sub-6 GHz applications with isolated n77/n78 bands using CSRR. *Phys. Scr.* **100**(1), 015508 (2024).

Author contributions

All authors contributed to the study conception and design. Material preparation, data collection and analysis were performed by S. Prasad Jones Christydass, DevakirubakaranSamithas, Praveen Kumar Balachandran and Muhammad AmmirrulAtiqi Mohd Zainuri. The first draft of the manuscript was written by S. Prasad Jones Christydass and all authors commented on previous versions of the manuscript. All authors read and approved the final manuscript.

Declarations

Competing interests

The authors declare no competing interests.

Additional information

Correspondence and requests for materials should be addressed to D.S. or P.K.B.

Reprints and permissions information is available at www.nature.com/reprints.

Publisher's note Springer Nature remains neutral with regard to jurisdictional claims in published maps and institutional affiliations.